Single grain virtualisation for contact behaviour analysis on sand

S. Nadimi[1], J. Fonseca*[2]

[1]PhD candidate; City, University of London, London, UK Sadegh.Nadimi-Shahraki@city.ac.uk

*[2]Corresponding author; Lecturer in Geotechnical Engineering; City, University of London, London, UK Joana.Fonseca.1@city.ac.uk

ABSTRACT

A methodology for virtualising irregular shaped grains is described here. The principle, largely inspired on Computed Tomography, is however, much simpler and accessible because only the 3D outline of the grain is required. The volumetric object is obtained by reconstructing the planar projections of the grain acquired at different angles of rotation using a standard camera. Depending on the lenses system, the resolution of the images can be as good as of a few microns. A numerical representation of the real grain can be obtained by meshing the 3D image. The influence of grain morphology on contact behaviour of a quartz sand is investigated here as an application for this novel technique. Numerical simulations using a finite-element model were carried out to reproduce the experimental data from normal compression single grain tests. The results show the contribution of the initial grain rearrangement on the normal force:displacement response and its strong dependency on the shape of the grain. This study demonstrates that particle shape is a critical parameter for calibration of contact behaviour of sand.

KEYWORDS: Particle scale behaviour; Image based geotechnics; Contact mechanics; Micro finite element.

INTRODUCTION

The mechanical behaviour of natural soil results from contact interaction of discrete grains (e.g. O'Sullivan, 2011; Fonseca *et al.*, 2016). The influence of grain morphology, including size and shape on the overall response of granular materials has been previously investigated by means of experimental and numerical methods (e.g. Oda & Iwashita, 1999; Lu & McDowell, 2007; Vlahinić *et al.*, 2014; Nguyen, *et al.*, 2015). There are, however, very few studies on the effect of single grain morphology and contact topology on contact interaction (Cavarretta *et al.*, 2010; Wang & Coop, 2016). Previous studies on single grain response have, for the most part, focused on the tensile strength and breakage potential of a single grain at high stress level (McDowell & Bolton, 1998;

Nakata *et al.*, 2001; Zhao *et al.*, 2015). Zhao *et al.* (2015) presented single grain compression of a few sand grains using micro-Computed Tomography (μCT) and noted that grain morphology and initial microstructure are the most important factors for determining the fracture pattern. For idealized particulate systems, Russell & Einav (2013) derived the energy dissipation due to fracturing of a single grain and by load redistribution in the surrounding grains. However the wide range of physical, numerical and analytical studies, single grain response has not been fully characterised yet. In particular, there is little understanding of the behaviour at low stress level.

It is expected that for irregular shapes under external applied load, disturbance of stress distribution within the grain will occur, which will affect the measured normal force:displacement response. The normal force:displacement relationship is critical for discrete modelling of soils. Hertzian theory provides the relation of normal force:displacement for two contacting spheres (Hertz, 1882), which constitutes a large simplification for representation of soil grains. This theory has been adopted in soil mechanics to model the discrete nature of soil (Cundall & Strack, 1979) and has been widely used since (O'Sullivan, 2011; Thornton, 2015).

For a large part of engineering applications, the maximum value of the contact forces in the assembly is believed to be lower than 10N (Cavarretta, 2009). At low stress level, it has been observed that the initial contact displacements are the result of damage of asperities (Greenwood & Tripp, 1967; Kendall, 1969). Greenwood & Tripp (1967) have shown that Hertzian response occurs only after a threshold load. Johnson *et al.* (1971) developed a new contact model based on these observations.

Asperities and contact topology are scale dependent parameters. Figs. 1a and 1b show a detailed contact between two sand grains (Terzaghi *et al.*, 1996) and the multiple asperities scale (Archard, 1957 cited in Greenwood & Wu, 2001). In soil mechanics, Cavarretta *et al.* (2010) quantified the surface roughness of sand grains and glass beads using an optical interferometer. The authors observed that the initial rotation of the grain together with asperity damage cause the pre-Hertzian response for irregular grains and concluded that the material response can be slightly dependant on the surface roughness, but the influence of grain shape is more significant. Altuhafi *et al.* (2016) reported that grain shape affects the intercept of the critical state line in the e:ln p' plane for low stress level. They also highlighted that shape has a strong effect on many aspects of sand behaviour, while the effect of roughness is more subtle.

In this paper, we investigate the effect of grain morphology on single grain response under compression. The methodology consists of capturing the morphology of the grain from the experimental test to be used in the numerical simulations with the aims of 1) calibrating discrete numerical simulations and 2) investigating the grain-scale parameters shaping the mechanical response. The outcome can contribute to the development of new contact laws considering the effect of grain morphology and asperities investigated here. Thus, enhancing discrete numerical simulations,

which includes conventional discrete element methods (DEM) and other approaches using deformable grains (e.g. Gethin et al, 2003; Komodromos & Williams, 2004; Nezamabadi et al., 2015; Nadimi & Fonseca; 2017). The morphology of the grain is obtained using a novel technique that uses 2D images of the grain to reconstruct the 3D shape. This technique, largely inspired from μCT, has the advantage of only requiring the use of a camera and other simple tools readily available in a geotechnical laboratory. The image acquisition is, however, limited to a grain at a time. In contrast with earlier studies that have considered breakage, this paper focuses on the behaviour of grains under low compression loads.

VIRTUALISATION OF A SINGLE GRAIN

This section describes the image acquisition system used to obtain the projections of the grain and the algorithm used to reconstruct the 3D images and subsequently generate the numerical mesh. The accuracy of the reconstruction algorithm was examined for artificial projections of a sphere.

Image acquisition system

The set-up developed to acquire the incremental rotation includes a camera, lens, remote controller, stepper motor (to rotate an object in controllable and precise increments), control kit, power supply and a set background. A schematic of the set-up is shown in Fig. 2.

The camera used is a digital SLR camera Canon EOS 60D 18 MP CMOS with EF-S 18-200mm lens and 65mm macro tube. A remote controller was used and shutter sound was muted to minimise any potential vibration. The motor is a hybrid, permanent magnet stepper motor with 0.9° step angle and 0.22Nm holding torque. The step angle accuracy is ±5%. The object to be imaged was mounted on the shaft of the motor using a tube with 0.5mm diameter and with a pedestal ending shape to make the contact area with the object as small as possible. The grain was glued to the ending point of the pedestal. The image resolution is controlled by the distance between the camera lens and the object. The 2D projections of the grain were acquired at various positions by rotating the step motor by an angle θ.

Volume reconstruction & mesh generation

Following image acquisition, the process of converting a real sand grain into a numerical grain comprises three main steps: image binarisation, volume reconstruction and mesh generation as detailed in the flowchart presented in Fig. 3. These operations were implemented using an in-house MATLAB (Mathworks, 2016) script with the rationale as follows. The binarisation process requires the selection of the features of interest in the image, the grain in this case. In order to extract the grain from the image, there was need to identify the pixels forming the grain and separate them from the pixels composing the background and the pedestal. The histogram of pixel intensity showed three clear peaks of higher intensities corresponding to the pixels composing the grain, the pedestal and the

background, respectively. Using Otsu's method (Otsu, 1979) the threshold value was obtained, below which pixels take value *0* (pedestal and background pixels) and above take value *1*, i.e. pixels forming the grain projection (grain area). A total of *N* binary images, each associated with a unique label *i* (varying between 1 and *N*) and a specific θ angle (acquisition angle), were used to reconstruct the 3D grain.

The algorithm for reconstruction consisted first, of extending (extruding) the grain projection from each binary image along a constant depth to form a cylinder with the cross section defined by the grain projection, for computational reasons the depth was taken as the largest dimension of the grain. The 3D grain was obtained from finding the intersection of all the *N* cylinders rotated by the cumulative angle of $(i-1)\times\theta$ according with the schematics shown in Fig. 4. Fig. 5 illustrates the reconstruction process of a sphere. In this case, it can be observed that using only the intersection of two cylinders (or projections) the overall 3D shape cannot be accurately captured (Fig. 5b), but as the number of projections increases to six (Fig. 5c) and subsequently to 30 (Fig. 5d), the 3D shape becomes progressively more refined. The optimal angle of rotation (θ) and number of projections needed to accurately capture the 3D outline is investigated later in this Section.

The numerical mesh used consisted of triangular elements at the surface and thetrahedral elements filling the inside of the grain. The surface mesh extraction technique used here is a refinement of the constrained Delaunay triangulation (Shewchuk, 2014). The quality of the mesh is controlled by three input parameters: 1) the element size at the surface, 2) the angle of the triangles and 3) the volume of the tetrahedrals.

Sensitivity analysis of the reconstruction method

The influence of the number of projections on the reconstructed 3D outline was investigated for the case of a standard spherical shape. Two sized spheres of 500µm and 1000µm diameter were considered, which corresponds to the size range of the sand grains used in this study. In both cases, a binary image of a circle with the diameter of the respective sphere was used as the planar projection (Figs. 5a and 6a). Both images have a resolution of 5µm, which means that the larger sphere has a more detailed definition (Figs. 5e and 6e). The analysis was carried out by comparing the real volume of the object (V_R) with the measured volume (V_M). The V_M was obtained by counting the voxels (volume pixels) in MATLAB. The evolution of the V_R/V_M ratio with the number of projections (and associated angle of rotation) is presented in Figs. 7a and 7b for the small and large spheres, respectively. The reconstructed shapes are also presented for the cases of 2, 6 and 30 projections in Figs. 5b,c,d and Figs. 6b,c,d, again for the small and large spheres, respectively. We can observe that using only two projections results in a very crude representation of the sphere (Fig. 6b) but the overall shape is well captured when the number of projections equals four, for which a volume ratio of approximately 0.95 was obtained (Fig. 7). The measured volume equals the real volume when the

number of projections equals 20 for the large sphere and 25 for the smaller sphere. Thus, 25 projections are used in this study.

The measured volume following meshing is also compared with the real volume for a coarse and a fine mesh (Figs. 7a and 7b). The V_M of the meshed volumes was measured in ABAQUS finite element package (Dassault Systèmes, 2014) using mass properties. As expected, a better agreement between the reconstructed and the meshed volumes is observed for the fine mesh. Using a coarse mesh seems, in this case, to underestimate the reconstructed volume for the small grain and overestimate for the larger grain (more detailed image). Nonetheless, we can say that the effect of meshing in the reconstructed volume is minimal.

SINGLE GRAIN COMPRESSION TESTS

This section describes the experimental and numerical single grain tests carried out on glass beads and Leighton Buzzard Sand (LBS). The spherical grains were used in order to compare the results against the well-established Hertz theory and thus provide a validation for the numerical and experimental modelling.

The experimental tests were carried out using the strain controlled machine '*Instron* 5969' (Instron ®), shown in Fig. 8. The instrumentation accuracy was measured to be <1μm for displacement and <0.1N for load. Prior to the experimental test, each grain was virtualised as described in the previous Section. A total of 25 projections, corresponding to an angle of rotation of 7.2˚, were acquired for each grain (N=25 and θ=7.2˚). In other words, each increment of rotation includes eight steps of 0.9 degree. The surface of the grain was cleaned with acetone before testing in order to remove any dust or glue remains.

Single grain tests on spherical beads

The nonlinear elastic relationship between the normal displacement and the normal contact force was computed using the simplified version of Hertz theory (Hertz, 1882) for two identical spheres in contact:

$$F_N = \iint_S \sigma_{yy} ds = F_{Hertz} = \frac{4}{3} E^* \sqrt{R} \delta_n^{\frac{3}{2}} \qquad \text{Eq. 1}$$

where E^* is the effective contact stiffness given by $E^* = E/(1-\vartheta^2)$, R is the sphere's radius, δ_n is the normal displacement, S denotes the contact area, E is the elastic modulus and ϑ is the Poisson's ratio.

This problem was reproduced in the framework of combined finite-discrete element model using dynamic explicit formulation by means of an explicit central difference time integration scheme (Munjiza, 2004; Nadimi & Fonseca, 2017). Due to symmetry, one sphere in contact with a rigid plate was simulated (Fig. 9). Physical and mechanical parameters of silica sand were assigned to the model, as listed in Table 1. The diameter of the sphere was defined based on the size of one of the LBS grains investigated here. Properties of hard contact were defined for the normal interaction. Due to deformation of the elastic sphere, the reaction force shows a nonlinear relationship with displacement as proposed by Hertz theory (Fig. 10a). A good agreement between the two curves can be observed for displacements lower than 30μm. Beyond this displacement value the numerical and theoretical responses start to diverge; which is due to the fact that Hertz solution is applicable only at small normal displacement (Vanimisetti & Narasimhan, 2006; Zheng *et al*., 2012). The internal stress field within the spherical grain, at the end of the test, shows a regular pattern of stress distribution as presented in Fig. 10b.

The experimental test was carried out on a single glass bead and the response was again compared with the theory to validate the set-up. The physical and mechanical properties of the glass bead used for the analytical solution are listed in Table 2. Fig. 11 illustrates the comparison between experiment and theory in terms of normal force:displacement, which shows excellent agreement and slightly stiffer response for displacement larger than 30μm in line with numerical simulations presented before.

Single grain tests on sand

Four LBS grains were randomly selected for this study. A view of the 3D outline after meshing, for each grain, is shown in Fig. 12. The nodes and elements were generated in MATLAB and imported into ABAQUS using an *.inp file containing the nodal coordinates and properties of all elements forming the mesh. The problem was solved using a dynamic explicit formulation mentioned above. The diameter (d) of each grain, as presented in Fig. 12, is defined here as the distance between the two horizontal platens used in the loading test. The geometrical resolution, or voxel size, used varies between 4-5μm depending on the distance of each grain to the camera. For the experimental test, the grain was placed in the loading system in a stable position which was recorded to better reproduce the grain position in the numerical domain, and thus, better replicate the experimental response.

The numerical simulations were carried out for the case of a purely elastic grain and also using an elastic-perfectly plastic constitutive model with a yield stress of 100MPa. To model these silica sand grains, the elastic modulus was assumed to be 100GPa and the Poisson's ratio of 0.22. Similarly with the experimental tests, for the numerical simulation, each grain was compressed between two rigid plates. Hard contact was assumed for contact interaction. The comparison of the experimental results

with the numerical response is presented in Fig. 13 for the elastic model. Similarly, the results of the experiments and the numerical elastic-plastic response are shown in Fig. 15.

DISCUSSION OF RESULTS

Referring to Fig. 13, we can see that for all cases the experimental results show an initial pre-Hertzian response as reported in the literature. A common feature in these four cases is the threshold load value of F_N=2.0N marking the transition from an initial pre-Hertzian response to a Hertzian like response. The corresponding displacement values (δ_i) for this transition point are however different for each grain. Displacement values of δ_i=16, 23, 91 and 11µm, respectively, for the grains LBS1, LBS2, LBS3 and LBS4, were measured. This initial displacement is believed to result from the effect of asperities and grain rotation in the experiments. Since asperity values measured for sand are less than 1.5µm (Cavarretta *et al.*, 2010; Altuhafi *et al.*, 2016); it can be concluded that contact roughness constitutes only a small contribution to δ_i and the larger effect comes from the initial rotation of the grain (due to the irregular shape of the grain, more precisely the top irregularity and the platen).

When comparing the numerical with the experimental results, and again, focusing on the pre-Herztian part of the curve, very good agreement is observed for grains LBS1, LBS2 and LBS4. This suggests that the level of detail of the images, which captures the overall form and not the asperities, can still provide a good prediction of the behaviour for very low stress level. This again supports the above hypothesis of the importance of shape over roughness. Grain LBS3 shows exceptionally high experimental initial displacement, δ_i= 151µm, and while the numerical prediction is also significantly large, δ_i= 91µm, the agreement is, however, less good (Fig. 13c). The explanation we offer is that the shape of this grain does not allow a clear stable position which contributes to: 1) further grain rotation during testing until two stable and near parallel contacts can be formed with the top and bottom platens, respectively and 2) difficulties in reproducing the position of the grain in the numerical simulation and thus, in capturing the experimental behaviour. To support this, the evolution of the stress distribution within the grain is analysed here. Fig. 14 shows the stress propagation from the top and bottom contact points at various load stages for grain LBS3 (through a vertical cut). The grain in the initial position before load was applied is shown in Fig. 14a, after 25mm displacement we can observe a small stressed area near the top and bottom contacts (Fig. 14b). As the applied force increases, the contacts are, however, lost due to rotation of the grain, resulting in an absence of stressed areas at this stage (Fig. 14c). With further increase in force and displacement, new contacts with new locations start to form as shown in Fig. 14d. These newly formed contacts are shown to be stable active contacts able to transmit forces higher than the threshold value (Figs. 14e and 14f).

From the normal force:displacement response for the elastic-perfectly plastic grain presented in Fig. 15, we can observe a softer numerical response when compared with the elastic formulation, and thus, a better agreement with the experimental results. This is expected since the quartz grains are inelastic.

Thus, using this finite-discrete element framework that allows introducing plasticity in the grain, presents significant advantages to more accurately capture the physical behaviour of the material. This will be further improved in future work by accounting for the tensile strength of the material to represent the drop in load using fracture mechanics criteria (*e.g.* Moes *et al.*, 1999; Borst, *et al.*, 2004). Finally, the internal stress distribution within the grain is shown for the final stage of loading to illustrate the disturbance in stress caused by the shape of the grain (Fig. 16).

CONCLUSION

A methodology was presented to calibrate contact behaviour to advance the numerical representation of grains in simulations using discrete approaches. The imaging set-up is very simple and easy to implement in any laboratory, thus presenting some advantages when compared with more sophisticated techniques such x-ray compute tomography. The ability of the acquisition method to capture the irregular 3D outline of a grain, enables it to be also used to quantify the size and shape of the grains (e.g. Fonseca et al., 2012; Sun et al., 2014). The analyses presented here demonstrate the suitability of the method for silica sand grains of approximately 1mm diameter. Larger and smaller grains can be used, with a compromise of a lower level of detail, i.e. larger grains better definition of the outline. By using virtualised Leighton Buzzard Sand grains in single grain numerical simulations, we have demonstrated the significance of the initial arrangement of the grain under normal compression for irregular shape grains. The numerical simulations presented here were able to capture almost perfectly the pre-Hertzian response of the grain, which is shown to be highly dependent on the shape of the grains and its ability to form stable contacts with the load platens. We have used the evolution of stress distribution within the grain throughout loading to demonstrate the role of initial particle rotation on the formation and disappearance of new contacts up to the formation of a stable active contact able to withstand the load until crack or breakage occurs. We therefore suggest that contact roughness is, for silica sand, of little significance when compared with the effect of contact topology to model contact behaviour. The developed codes for grain virtualisation and image based meshing will be available at http://openaccess.city.ac.uk/ for download.

ACKNOWLEDGMENT

The authors would like to thanks City University of London for the doctoral scholarship of the first author.

REFERENCES

ABAQUS User's Manual 2014. Dassault Systèmes, version 6.14.

Altuhafi, F., Coop, M., & Georgiannou, V. 2016. Effect of Particle Shape on the Mechanical Behaviour of Natural Sands." *J. Geotech. Geoenviron. Eng.*, 10.1061/(ASCE)GT.1943-5606.0001569, 04016071.

Archard, J.F. 1957. Elastic deformation and the laws of friction. *Proc. Roy. Soc.* **A243**: 190–205.

Borst, R. d., Remmers, J. J. C., Needleman, A. and Abellan, M.-A. (2004), Discrete vs smeared crack models for concrete fracture: bridging the gap. *Int. J. Numer. Anal. Meth. Geomech.,* **28**: 583–607.

Cavarretta, I. 2009. *The influence of particle characteristics on the engineering behaviour of granular materials*. PhD Thesis, Imperial College London.

Cavarretta, I., Coop, M. & O'Sullivan, C. 2010. The influence of particle characteristics on the behaviour of coarse grained soils. *Géotechnique* **60** (6): 413-423.

Cundall, P.A. & Strack, O.D.L. 1979. A discrete numerical model for granular assemblies. *Géotechnique* **29**:1, 47-65.

Fonseca, J., O'Sullivan, C., Coop, M.R. & Lee, P.D. 2012. Non-invasive characterization of particle morphology of natural sands. *Soils and Foundations* **52** (4): 712-722.

Fonseca, J., O'Sullivan, C., Coop, M. R., & Lee, P. D. 2013a. Quantifying the evolution of soil fabric during shearing using directional parameters. *Géotechnique* **63**(6), 487-499.

Fonseca, J., O'Sullivan, C., Coop, M.R. & Lee, P.D. 2013b. Quantifying the evolution of soil fabric during shearing using scalar parameters. *Géotechnique* **63** (10): 818-829.

Fonseca, J., Nadimi, S., Reyes-Aldasoro, C.C, O'Sullivan, C. & Coop, M.R. 2016. Image-based investigation into the primary fabric of stress transmitting particles in sand. *Soils & Foundations* **56**(5): 818-834.

Gethin, D.T., Lewis, R.W. & Ransing, R.S. (2003). A discrete deformable element approach for the compaction of powder systems. *Modelling Simul. Mater. Sci. Eng.* **11** 101.

Greenwood, J. A. & Tripp, J. H. 1967. The Elastic Contact of Rough Spheres. *Journal of Applied Mechanics. Transactions of the American Society of Mechanical Engineers* **34**, No. 1, 153-159.

Greenwood, J.A. & Wu, J.J. 2001. Surface Roughness and Contact: An Apology. *Meccanica* **36**: 617–630.

Hertz, H. 1882. Über die Berührung fester elastischer Körper. *J. reine und angewandte Mathematik* **92**: 156- 171.

Instron ®, ITW Test & Measurement, UK

Johnson, K. L., Kendall, K. & Roberts A. D. 1971. Surface energy and the contact of elastic solids. *Proceedings of the Royal Society of London. Series A, Mathematical and Physical Sciences* **324**, No 1558, 301-313.

Kendall, K. 1969. The stiffness of surfaces in static and sliding contact. Ph. D. thesis, University of Cambridge, Engineering Department, Pembroke College.

Komodromos, P.I. and Williams, J.R. (2004) 'Dynamic simulation of multiple deformable bodies using combined discrete and finite element methods', *Engineering Computations*, **21**(2/3/4), pp. 431–448. doi: 10.1108/02644400410510875.

Lu, M., & McDowell, G.R. 2007. The importance of modelling ballast particle shape in the discrete element method. *Granular Matter* **9** (1): 69-80.

MATLAB (2016). version 9.0 (R2016a). The MathWorks Inc., Natick, Massachusetts.

McDowell, G.R. & Bolton, M.D. 1998. On the micromechanics of crushable aggregates. *Géotechnique* **48**(5): 667-679.

Moes, N., Dolbow, J. & Belytschko, T. (1999). A finite element method for crack growth without remeshing. *International Journal for Numerical Methods in Engineering* **46**:131-150.

Munjiza, A. 2004. *The combined finite-discrete element method*. West Sussex, England: John Wiley & Sons.

Nadimi, S. & Fonseca, J. (2017). A micro finite element model for soil behaviour. II: particle morphology and contact topology. *Géotechnique* (under review, Jan 2017). Nakata, Y., Kato, Y.,

Nezamabadi, S., Radjai, F., Averseng, J., & Delenne, J. Y. (2015). Implicit frictional-contact model for soft particle systems. *Journal of the Mechanics and Physics of Solids* **83**: 72-87.

Hyodo, M., Hyde, A.F.L. & Murata, H. 2001. One-dimensional compression behaviour of uniformly graded sand related to single particle crushing strength. *Soils & Foundations* **41**(2): 39-51.

Nguyen, D., Azéma, E., Sornay, P. & Radjai, F. 2015. Effects of shape and size polydispersity on strength properties of granular materials. *Physical Review E* **91**, 032203.

Oda, M. & Iwashita, K. 1999. Mechanics of granular materials, an introduction. Rotterdam, the Netherlands CRC Press.

O'Sullivan, C. 2011. *Particulate Discrete Element Modelling: A Geomechanics Perspective*. Spon Press.

Otsu, N. 1979. A Threshold Selection Method from Gray-Level Histograms. *IEEE Transactions on Systems*, Man, and Cybernetics, Vol. 9, No. 1, pp. 62-66.

Russell, A.R. & Einav, I. 2013. Energy dissipation from particulate systems undergoing a single particle crushing event. *Granular Matter* **15**:299-314.

Shewchuk, J. R. 2014. Reprint of: Delaunay refinement algorithms for triangular mesh generation. *Computational Geometry: Theory and Applications* **47**(7): 741-778.

Sun, Y., Indraratna, B., & Nimbalkar Dr, S. 2014. Three-dimensional characterisation of particle size and shape for ballast. *Géotechnique Letters* 4: 197-202.

Terzaghi, K., Peck, R.B. & Mesri, G. 1996. *Soil Mechanics in Engineering Practice, 3rd Edition*. John Wiley & Sons. ISBN: 978-0-471-08658-1.

Thornton, C. 2015. *Granular Dynamics, Contact Mechanics and Particle System Simulations*. Springer International Publishing.

Vanimisetti, S. K. & Narasimhan, R. 2006. A numerical analysis of spherical indentation response of thin hard films on soft substrates, *International Journal of Solids and Structures*, **43**(20): 6180-6193, http://dx.doi.org/10.1016/j.ijsolstr.2005.05.032.

Vlahinić, I., Andò, E., Viggiani, G., Andrade, J.E. (2014). Towards a more accurate characterization of granular media: extracting quantitative descriptors from tomographic images. *Granular Matter* **16** (1): 9-21.

Wang, W. & Coop, M.R. 2016. An investigation of breakage behaviour of single sand particles using a high-speed microscope camera. *Géotechnique*, http://dx.doi.org/10.1680/jgeot.15.P.247.

Zheng, Q.J., Zhu, H.P. & Yu, A.B. 2012. Finite element analysis of the contact forces between a viscoelastic sphere and rigid plane, *Powder Technology* **226**: 130–142.

Zhao, B. Wang, J. Coop, M.R. Viggiani, G. & Jiang, M. 2015. An investigation of single sand particle fracture using X-ray micro-tomography. *Géotechnique* **65**(8): 625-641.

Table 1. Physical and mechanical properties used in the numerical simulations of silica sand

Elastic Modulus	100	GPa
Poisson's ratio	0.22	-
Diameter	0.815	mm

Table 2. Physical and mechanical properties used for the analytical solution of glass beads

Elastic Modulus	63	GPa
Poisson's ratio	0.22	-
Diameter	2.15	mm

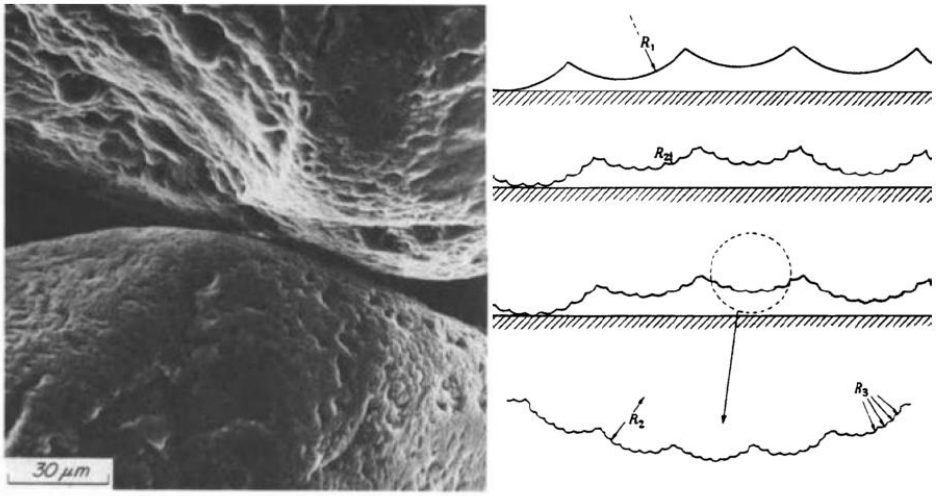

Fig. 1. (a) Micrograph of contact between grains of quartz sand (Terzaghi et al., 1996) (b) Example of multiple roughness scales (Archard, 1957 cited in Greenwood & Wu, 2001).

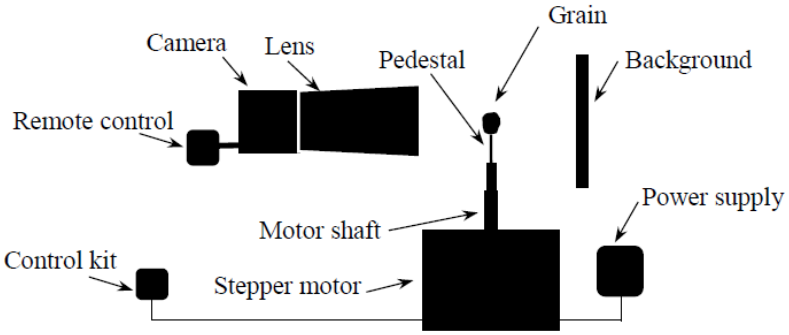

Fig. 2. Schematic of the set-up used for image acquisition.

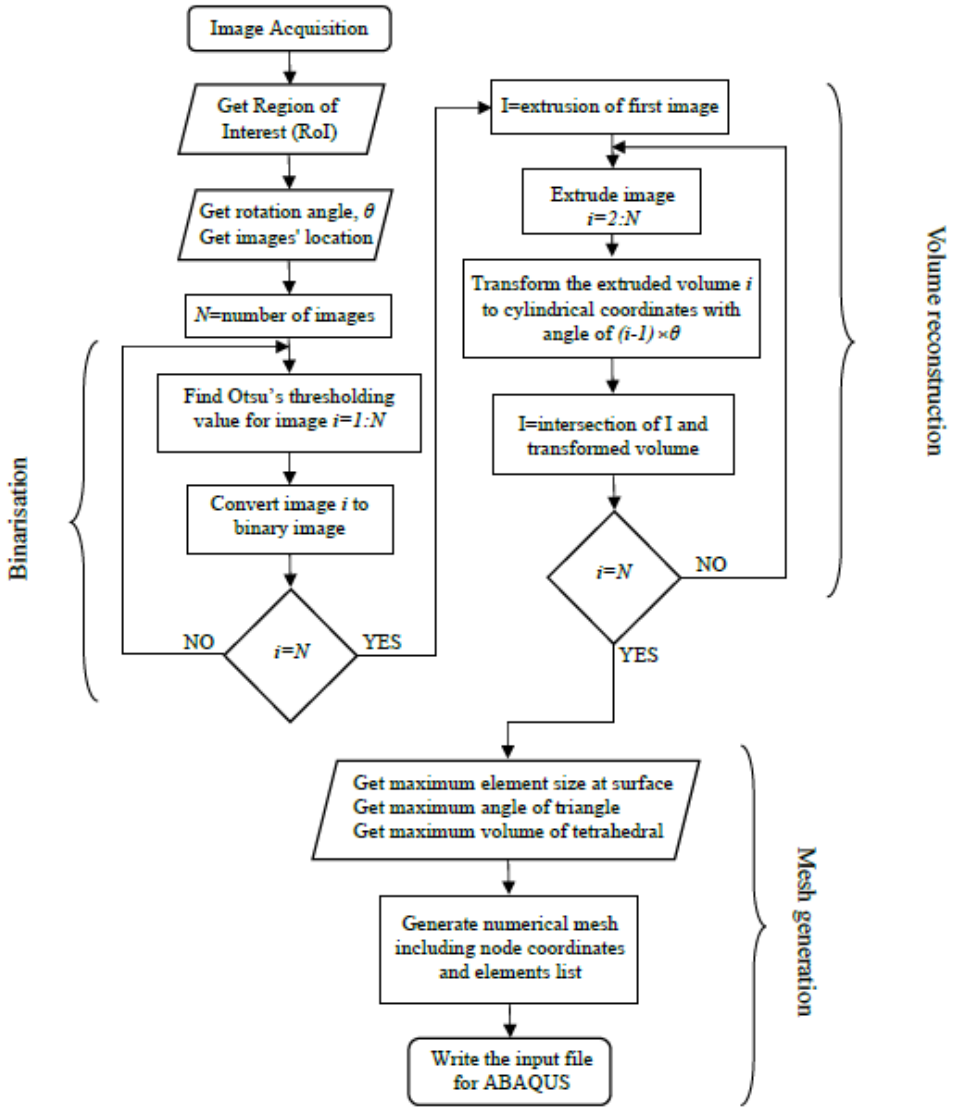

Fig. 3. Flowchart illustrating the algorithms used for volume reconstruction and meshing.

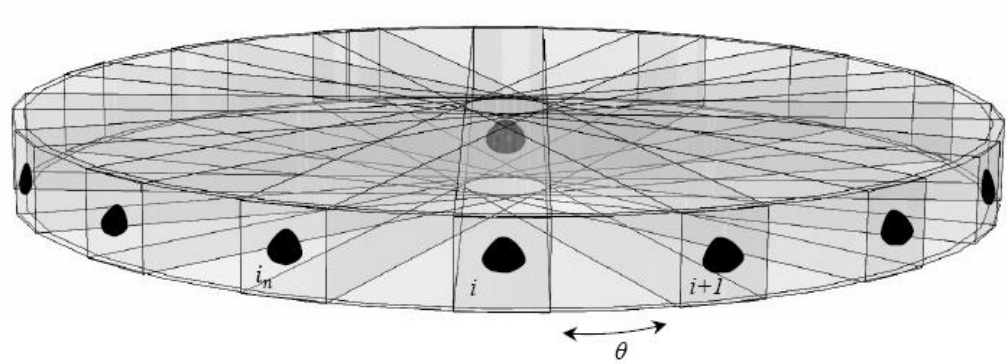

Fig. 4. Schematics of the incremental projection method used to reconstruct the 3D volume.

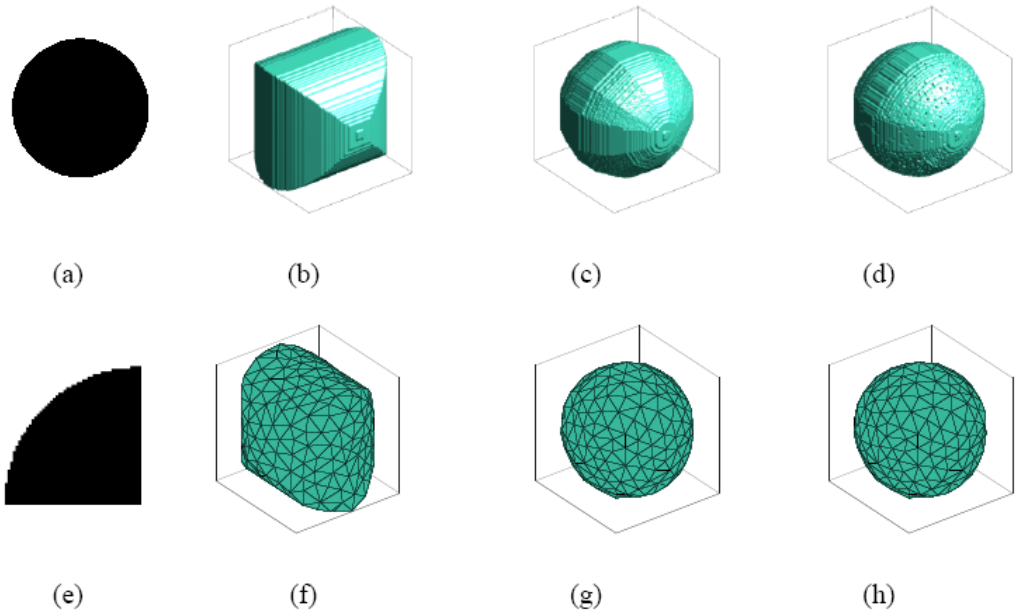

Fig.5. Reconstruction of a sphere with 500 µm diameter (a) planar projection, (b) reconstructed volume (RV) using 2 projections, (c) RV using 6 projections, (d) RV using 30 projections, (e) zoomed view of (a), (f) coarse meshed volume (CMV) of (b), (g) CMV of (c), (h) CMV of (d).

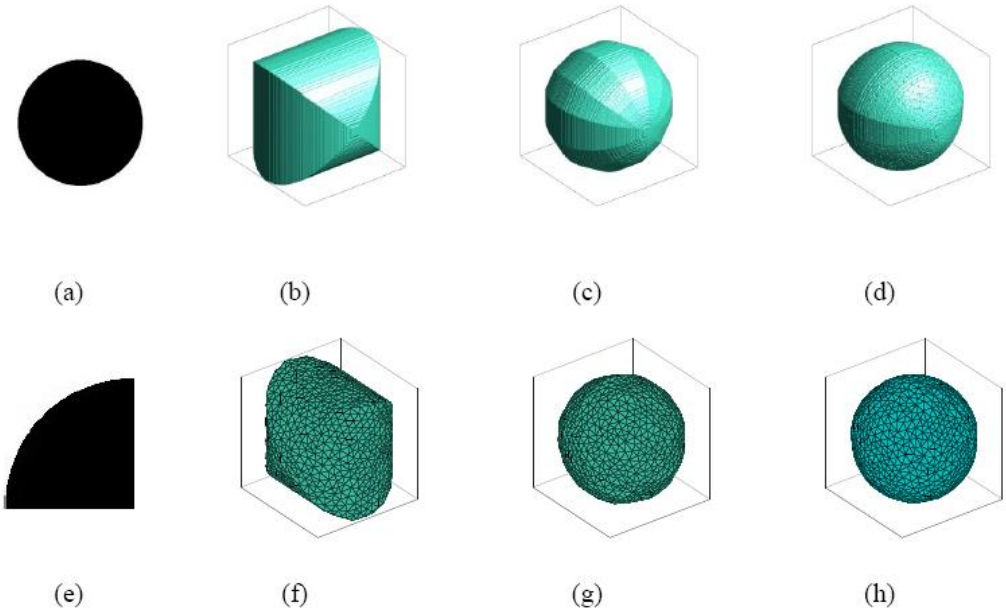

Fig. 6. Reconstruction of a sphere with 1000 µm diameter (a) planar projection, (b) reconstructed volume (RV) using 2 projections, (c) RV using 6 projections, (d) RV using 30 projections, (e) zoomed view of (a), (f) coarse meshed volume (CMV) of (b), (g) CMV of (c), (h) CMV of (d).

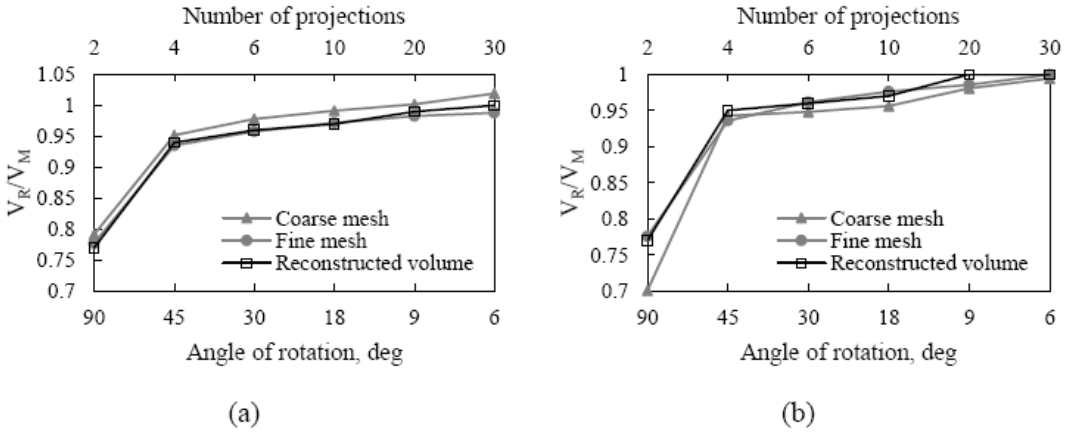

Fig. 7. Evolution of the ratio between the real volume (V_R) and the measured volume (V_M) for a sphere with (a) 500µm diameter (b) 1000µm diameter.

Fig. 8. Set-up used for the single grain experiments.

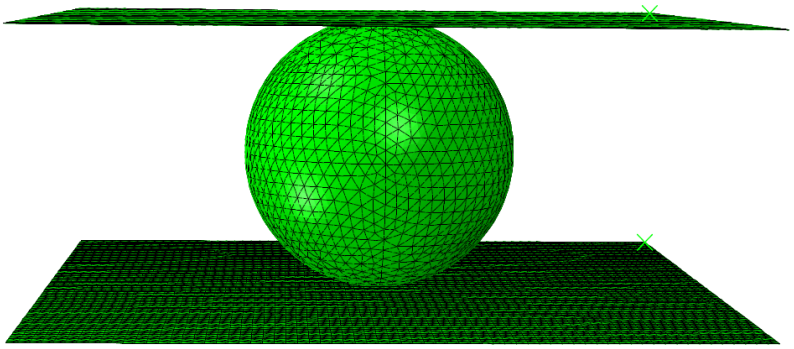

Fig. 9. Geometry and mesh of a sphere in contact with two rigid plates.

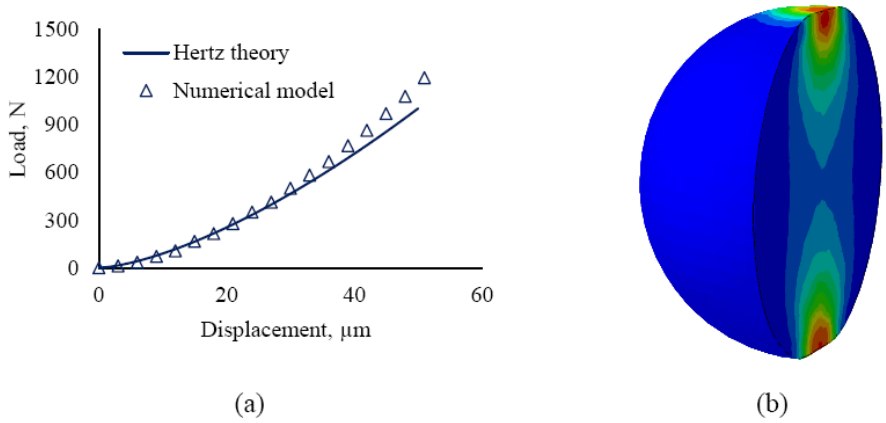

Fig. 10. (a) Comparison between numerical modelling and Hertz theory for a single grain under compression, (b) Internal stress distribution in a sphere.

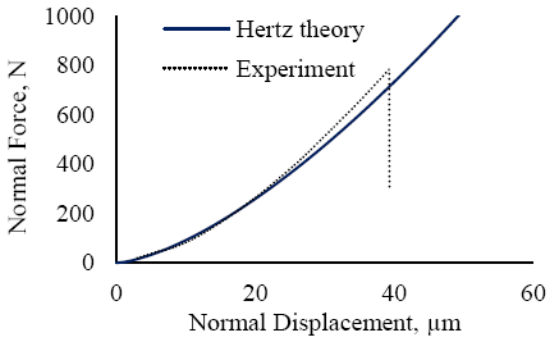

Fig. 11. Single grain response of glass beads from Hertz theory and experimental tests.

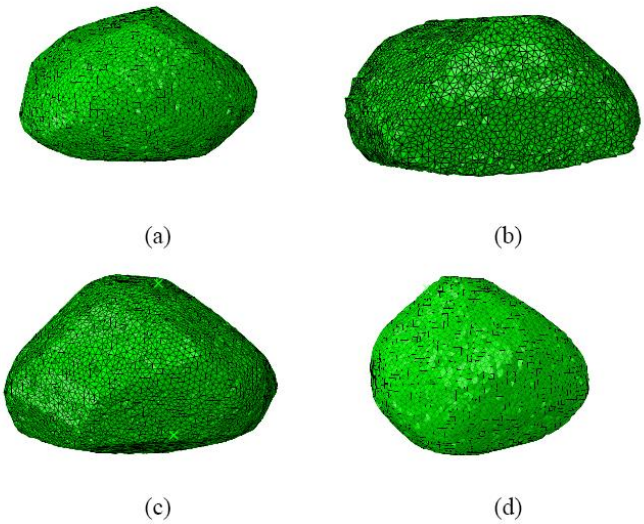

Fig. 12. Illustration of the four grains tested and the corresponding measured diameter (*d*): (a) LBS1, *d*=815μm≈200voxel (b) LBS2, *d*=1064μm≈226voxel, (c) LBS3, *d*=1073μm≈253voxel, (d) LBS4, *d*=1042μm≈254voxel.

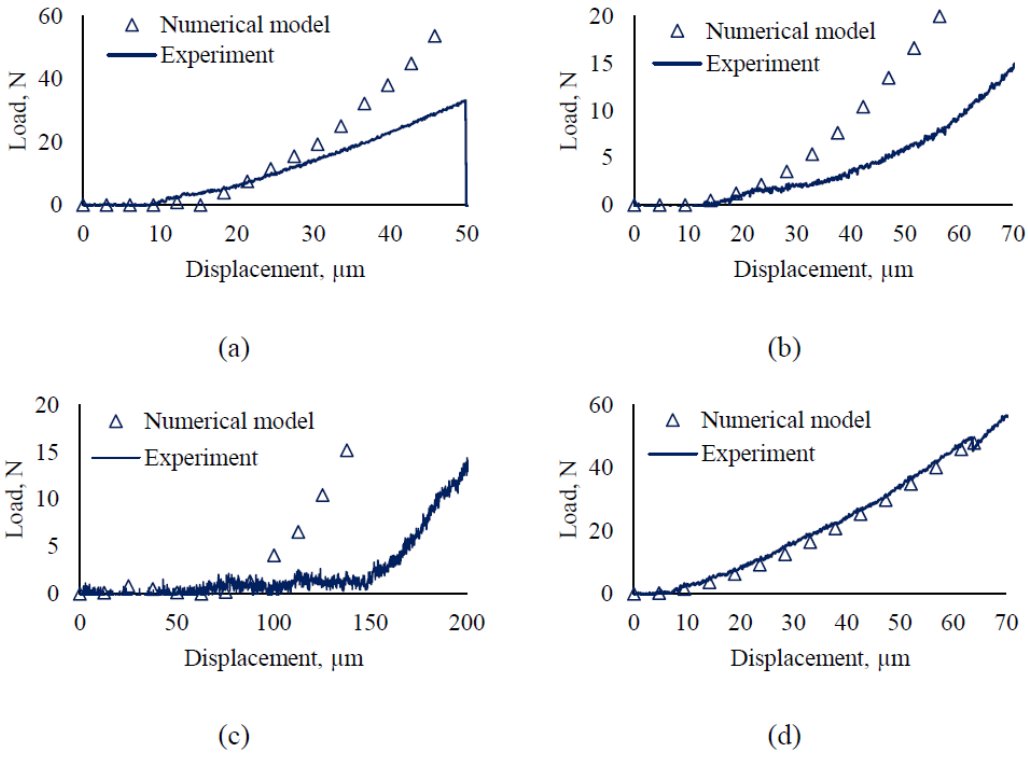

Fig. 13. Normal force displacement response from elastic numerical simulations and experimental tests for: (a) LBS1, (b) LBS2, (c) LBS3, (d) LBS4.

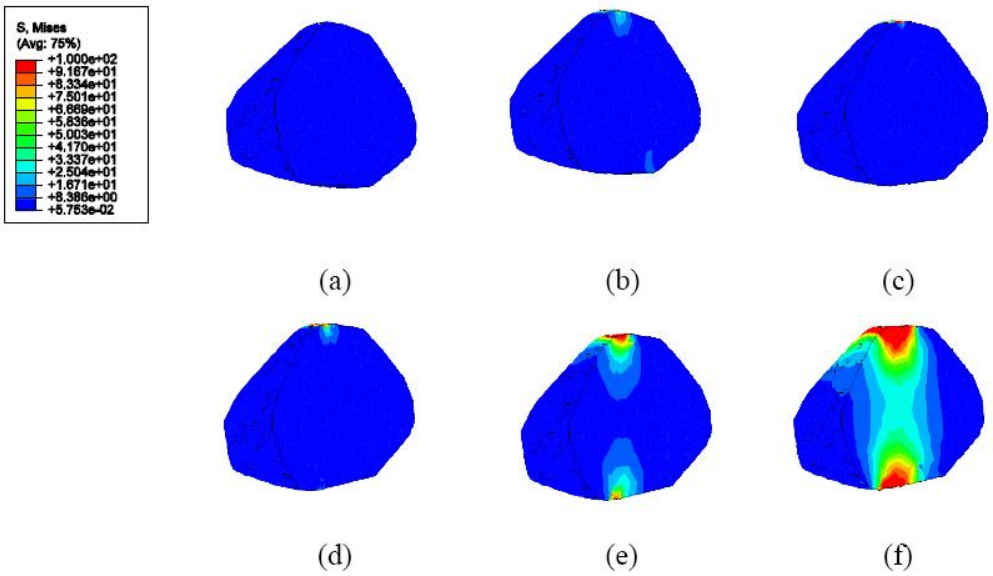

Fig. 14. Stress distribution within grain LBS3 at different loading stages, through a vertical section: (a) Disp.= 0µm, FN=0N; (b) Disp.= 25µm, FN=0.82N; (c) Disp.= 50µm, FN=0.12N; (d) Disp.= 75µm, FN=0.19N; (e) Disp.= 100µm, FN=4.07N; (f) Disp.= 125µm, FN=10.47N

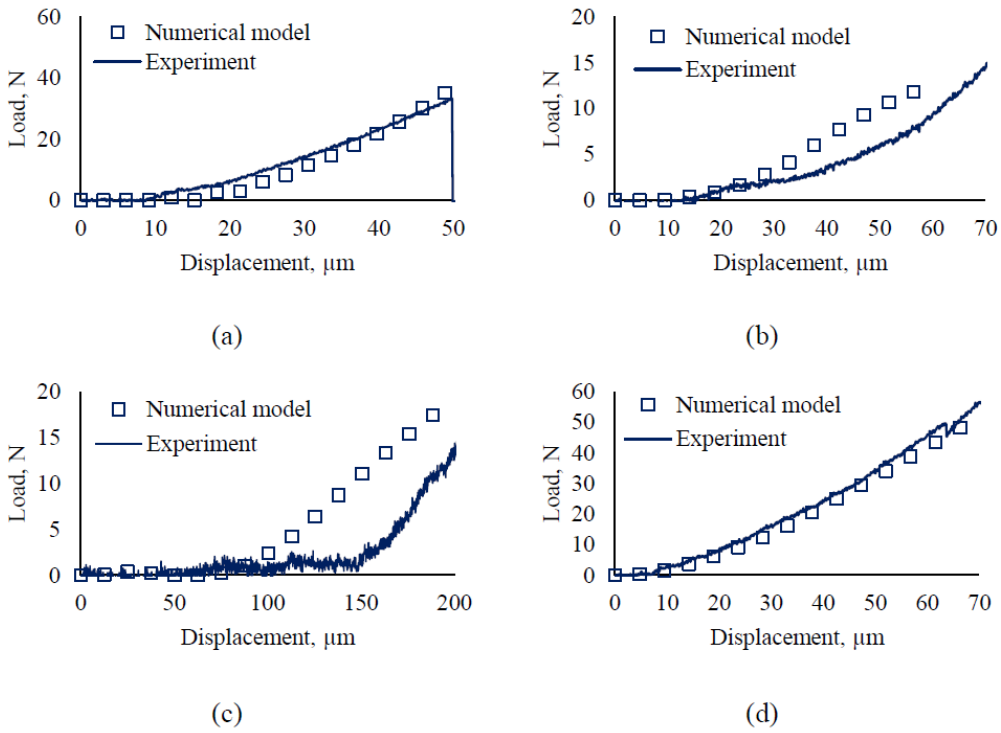

Fig. 15. Normal force displacement response from plastic numerical simulations and experimental tests for: (a) LBS1, (b) LBS2, (c) LBS3, (d) LBS4.

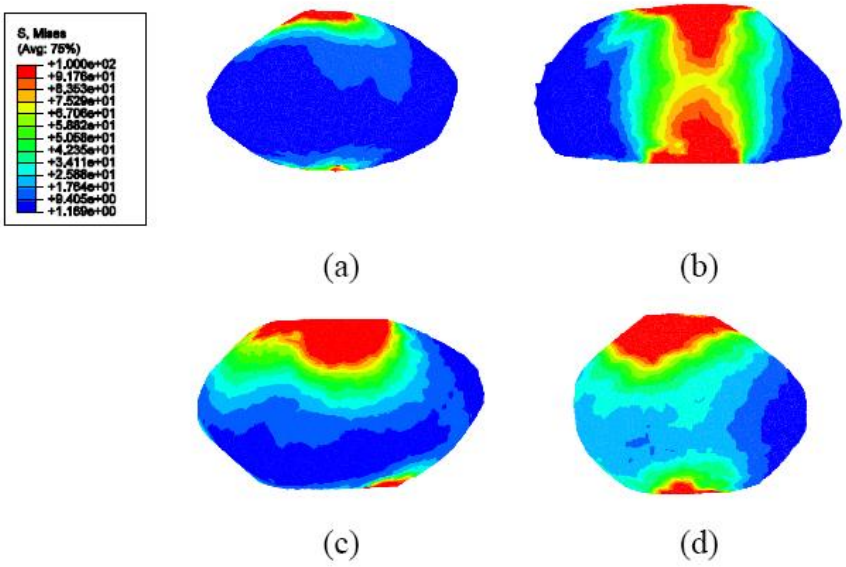

Fig. 16. Stress distribution obtained at the end of the elastic-plastic simulation for: (a) LBS1, (b) LBS2, (c) LBS3, (d) LBS4.